CHEMISTRY

# Optimizing selectivity via membrane molecular packing manipulation for simultaneous cation and anion screening

**Qing-Wei Meng[1]†, Jianguo Li[2]†, Zhuozhi Lai[1], Weipeng Xian[1], Sai Wang[1], Fang Chen[1], Zhifeng Dai[2], Li Zhang[2]*, Hong Yin[1], Shengqian Ma[3], Qi Sun[1]***



**Advancing membranes with enhanced solute-solute selectivity is essential for expanding membrane technology applications, yet it presents a notable challenge. Drawing inspiration from the unparalleled selectivity of biological systems, which benefit from the sophisticated spatial organization of functionalities, we posit that manipulating the arrangement of the membrane's building blocks, an aspect previously given limited attention, can address this challenge. We demonstrate that optimizing the face-to-face orientation of building blocks during the assembly of covalent-organic-framework (COF) membranes improves ion-π interactions with multivalent ions. This optimization leads to extraordinary selectivity in differentiating between monovalent cations and anions from their multivalent counterparts, achieving selectivity factors of 214 for $K^+/Al^{3+}$ and 451 for $NO_3^-/PO_4^{3-}$. Leveraging this attribute, the COF membrane facilitates the direct extraction of NaCl from seawater with a purity of 99.57%. These findings offer an alternative approach for designing highly selective membrane materials, offering promising prospects for advancing membrane-based technologies.**

## INTRODUCTION

The development of membranes with enhanced solute-solute selectivity is crucial for applications in energy storage, environmental cleanup, and sustainable industrial practices (*1*–*16*). Achieving precise ion discrimination is a key challenge in many of these processes. A prevalently adopted method involves modifying membranes with charged functional groups to facilitate selective ion passage, cations through positively charged membranes and anions through negatively charged ones, leveraging the Donnan effect (*17*–*21*). However, designing membranes that efficiently filter both cations and anions, which could streamline separation processes, remains a notable challenge. Janus membranes, recognized for their asymmetrically charged surfaces, offer a potential solution for this dual filtration (*22*–*28*). Nonetheless, their wider implementation is restricted by complex fabrication methods and generally lower ion flux rates compared to other membrane varieties. As such, continued innovation in membrane technology is essential for improving the selectivity and efficiency of ion separation processes.

In the realm of biological recognition, protein channels demonstrate exceptional specificity in transporting substances across cellular membranes, with non-covalent interactions, especially those involving π systems, playing a pivotal role (*29*–*32*). The distinct quadrupole moment of aromatic rings leads to a unique charge distribution, featuring a partial negative charge across the π system and a partial positive charge encircling the aromatic ring (*33*). This configuration enables interactions with both positively and negatively charged ions. Although the interaction between an aromatic molecule and ions is generally weak, strategically aligning multiple π systems can greatly enhance these interactions, thus improving selectivity. Aromatic foldamers are a prime example, showcasing exceptional ion transport selectivity by organizing aromatic molecules into specific configurations that have unique dielectric surface properties, essential for selective ion transport through various π-interactions (*34*–*38*). Despite the progress, a notable research gap remains in leveraging this understanding to develop synthetic membranes for ion separation. Addressing this gap involves manipulating the orientation of aromatic building blocks during the membrane formation process, with the expectation that the resulting membrane will demonstrate remarkable selectivity.

In this study, we explored the potential of two-dimensional covalent organic frameworks (2D COFs) to bring our concept to fruition. These frameworks are designed to organize molecular components into a periodic, crystalline, layered 2D array, providing expansive surface areas and exceptional stability (*39*–*52*). The defining feature of these 2D materials is their stacked functional π-electron systems, positioned in close proximity to maximize van der Waals interactions and ensure optimal π-orbital overlap. Moreover, these frameworks are distinguished by their open, porous channels that align with the direction of stacking. Analogous to π-stacked foldamers, which are electrically neutral on the whole, these channels are predicted to exhibit a negatively charged exterior and a positively charged interior, facilitating the hypothesis that an oriented COF membrane could efficiently separate both cations and anions through diverse ion-π interactions with the aligned aromatic systems (Fig. 1). Our findings confirmed that the oriented COF membrane, even without specific functional groups, exhibited exceptional selectivity, distinguishing monovalent cations and anions from their multivalent counterparts, with selectivity factors reaching up to 214 ($K^+/Al^{3+}$) and 451 ($NO_3^-/PO_4^{3-}$), respectively. Given the structural similarity within the realm of 2D COFs, we anticipate that these selectivities are indicative of the entire class of materials.

[1]Zhejiang Provincial Key Laboratory of Advanced Chemical Engineering Manufacture Technology, College of Chemical and Biological Engineering, Zhejiang University, Hangzhou 310027, China. [2]Key Laboratory of Surface and Interface Science of Polymer Materials of Zhejiang Province, School of Chemistry and Chemical Engineering, Zhejiang Sci-Tech University, Hangzhou 310018, China. [3]Department of Chemistry, University of North Texas, 1508 W Mulberry St., Denton, TX 76201, USA. *Corresponding author. Email: sunqichs@zju.edu.cn (Q.S.); lizhang@zstu.edu.cn (L.Z.)
†These authors contributed equally to this work.

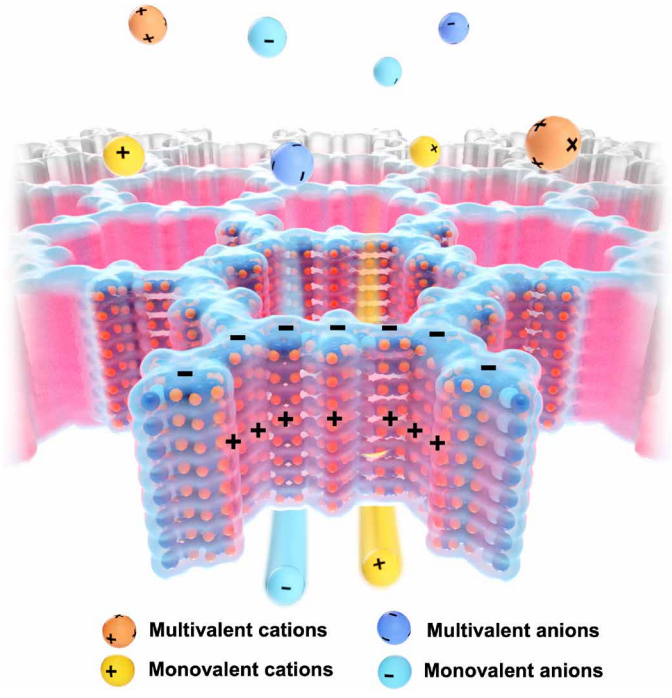


**Fig. 1. Conceptual design.** Graphic representation depicting the charge allocation in a 2D COF membrane with eclipsed AA stacking, engineered for simultaneous screening of anions and cations.

## RESULTS

### Membrane preparation and characterization

Leveraging the stability and controllability offered by the Schiff base condensation reaction for COF synthesis (*53*–*61*), we opted for 1,3,5-tris (4-aminophenyl)-benzene (Tab) and 2,5-divinylterephthalaldehyde (Dva) as building blocks in our proof-of-concept study. This choice was intended to avoid the introduction of heteroatoms (N, O, F, etc.) that might generate negative electrostatic potential (ESP) (*62*) while leveraging the adjustable crystallinity and orientation of the COF membrane synthesized from Tab. The combination of Tab and vinyl-substituted aldehyde was anticipated to enhance packing efficiency. To examine the charge distribution within the COF material, molecular ESP analyses were conducted. Given the periodic nature of the COF structure, our analysis focused on a singular hexagonal macrocycle to elucidate charge distribution intricacies. The findings revealed a notable positive partial charge oriented along the direction of pore channels, juxtaposed with negatively charged pore surfaces, in line with our proposed model (Fig. 2A).

Liquid-solid interfacial polymerization was used in the membrane synthesis process, involving the dissolution of monomers in an organic solvent and the dispersion of $Sc(OTf)_3$ catalyst in an aqueous phase (fig. S1). Control over membrane thickness was achieved by modulating the concentrations of monomers and catalyst. Site-specific polymerization facilitated membrane formation on the tube wall, resulting in self-sustaining membranes that could be readily detached from the tube wall via a brief base treatment (0.05 M KOH). These membranes exhibited visually distinct hues, blue-purple and yellow, indicative of varying thicknesses, following the principle of thin film interference (Fig. 2, B and C, inset). Further analysis through scanning electron microscopy (SEM) cross sections revealed that the blue-purple and yellow membranes had thicknesses of 170 and 976 nm, respectively (Fig. 2, B and C, and figs. S2 and S3). Therefore, these



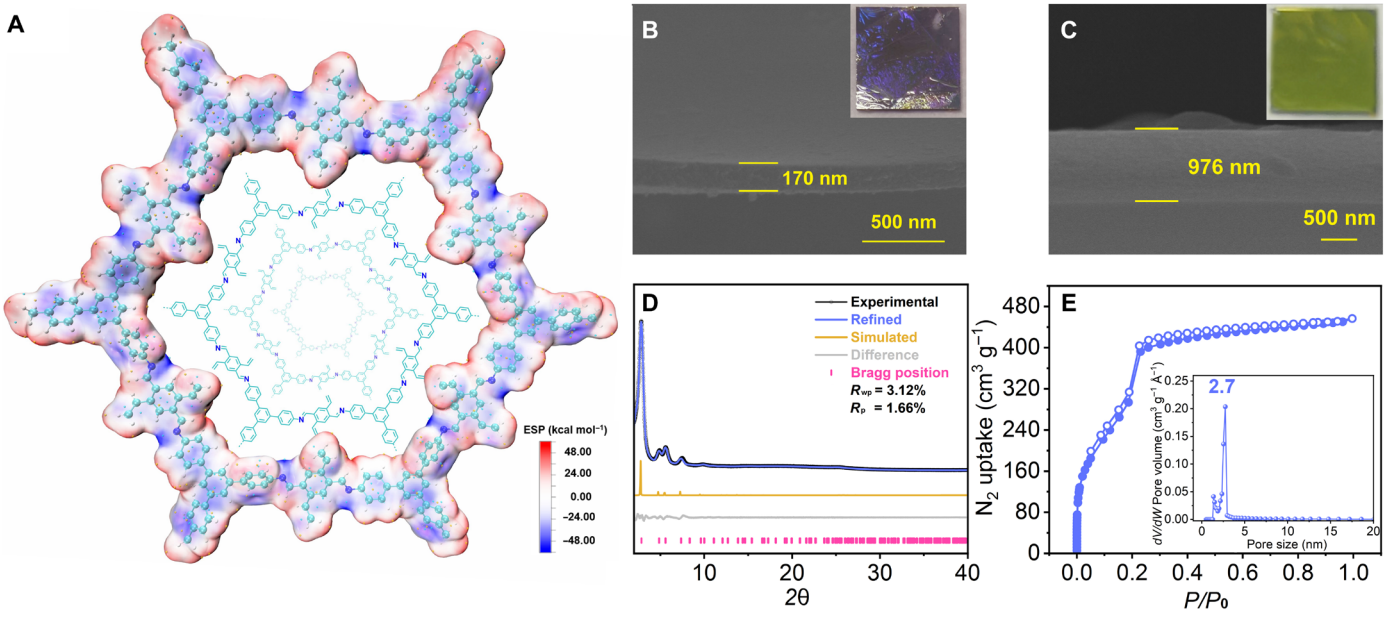


**Fig. 2. ESP distribution and characterizations of the COF-170 membrane.** (**A**) Visualization of the molecular ESP for an individual hexagonal macrocycle within the COF constructed from Tab and Dva. (**B** and **C**) Scanning electron microscopy (SEM) images capturing the structures of COF-170 and COF-976, complemented by insets displaying their corresponding digital photos on Si wafers. (**D** and **E**) Presentation of the powder x-ray diffraction (PXRD) pattern and $N_2$ sorption isotherms for the COF-170 membrane, with an inset depicting the pore size distribution. $R_{wp}$, $R_{weighted\ pattern}$; $R_p$, $R_{pattern}$.

membranes were denoted as COF-170 and COF-976, respectively. The COF-170 membrane was chosen as a representative sample for comprehensive characterization. The evidence of Schiff-base condensation was verified by observing the characteristic C═N peaks at 1608 $cm^{-1}$ in the Fourier transform infrared (FTIR) spectrum and at 157.1 parts per million in the solid-state $^{13}C$ nuclear magnetic resonance spectrum (figs. S4 and S5) (*63*). Powder x-ray diffraction (PXRD) analysis of the finely ground COF membrane displayed distinct diffraction peaks closely aligned with a simulated pattern based on an AA eclipsed stacking configuration, signifying an excellent macroscopic crystallinity (fig. S6). This configuration linked Tab and Dva units in periodic connections, creating hexagonal formations that extended into 2D polymeric layers. These layers stacked in an eclipsed manner, forming 1D mesoporous channels (Fig. 2D and table S1). Transmission electron microscopy (TEM) further illuminated structural details, revealing honeycomb-patterned pores oriented along the [001] direction, featuring a d100 spacing of 2.7 nm (fig. S7). The AA eclipsed stacking model found further support in $N_2$ sorption isotherms. The membrane exhibited a Brunauer-Emmett-Teller surface area of 1725 $m^2 g^{-1}$, predominantly featuring a pore size distribution around 2.7 nm estimated using the slit-pore model (fig. S8). These findings align with the predicted pore size (2.7 nm) from the eclipsed model (Fig. 2E).

## Examining of the influence of membrane orientation on ion selectivity

To assess ion permeability across COF membranes, we initially investigated individual salts—NaCl, $Na_2SO_4$, and $MgCl_2$—at a concentration of 0.1 M, representing mono/multivalent cations and anions. For enhanced operational stability, these membranes were transferred onto polyacrylonitrile (PAN) ultrafiltration membranes. We selected PAN due to its cost-effectiveness and broad availability, which is advantageous given that our separation system does not require exposure to strong acids, bases, or harsh organic solvents. Nonetheless, the resulting freestanding membrane could potentially be applied to any porous substrate. The resulting composite membranes (COF-170/PAN and COF-976/PAN) underwent evaluation in H-type diffusion cells to quantify salt transmembrane activity, with a conductivity meter employed for accurate measurements. In a control experiment using only the PAN membrane, salt fluxes for NaCl, $Na_2SO_4$, and $MgCl_2$ were recorded at 130, 102, and 96 mmol $m^{-2}$ $hour^{-1}$, respectively, showing little preference among these salts as their selectivities were similar to their diffusion coefficients ratios (Fig. 3A and figs. S9 and S10). Conversely, the COF-170/PAN membrane exhibited selectivities of 62 for $Cl^-/SO_4^{2-}$ and 17 for $Na^+/Mg^{2+}$, outperforming the commercial polyamide nanofiltration membrane (NF-270 from Dow Corp.), which demonstrated selectivities of 6.4 for $Cl^-/SO_4^{2-}$ and 21.0 for $Na^+/Mg^{2+}$. Comparative analysis of the salt transmembrane behavior of COF-170/PAN and COF-976/PAN membranes revealed that an increase in membrane thickness resulted in a decrease in NaCl flux (from 90 to 20 mmol $m^{-2}$ $hour^{-1}$). In contrast, there was an increase in $Na_2SO_4$ and $MgCl_2$ flux (from 1.5 to 10 mmol $m^{-2}$ $hour^{-1}$ for $Na_2SO_4$ and from 5.3 to 9.1 mmol $m^{-2}$ $hour^{-1}$ for $MgCl_2$). Consequently, the selectivity for $Cl^-/SO_4^{2-}$ and $Na^+/Mg^{2+}$ notably decreased from 62 to 2 and from 17 to 2.2, respectively.

To elucidate this anomalous experimental phenomenon, we applied small-angle x-ray scattering (SAXS) and synchrotron grazing-incidence wide-angle x-ray scattering (GIWAXS) techniques to analyze the crystallinity and orientation and thereby the packing of the building blocks of the COF-170 and COF-976 membranes. The SAXS patterns of both membranes exhibited high crystallinity, with their diffraction peaks showing similar characteristics (Fig. 3, B to E). A notable observation was that the 100 diffraction peak of

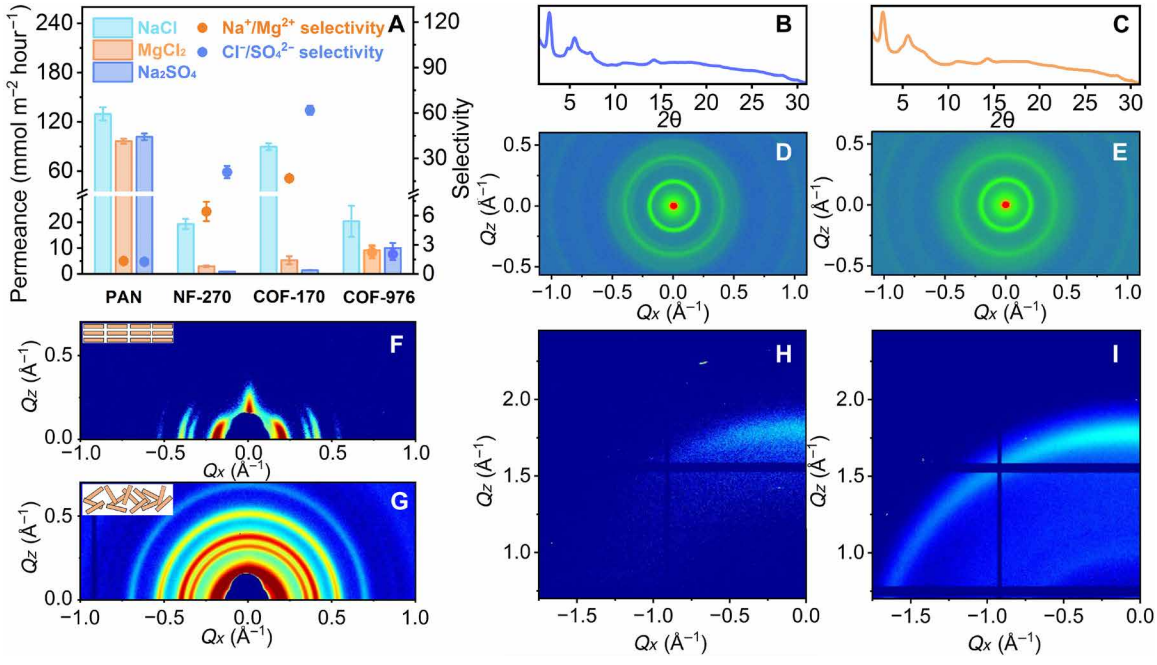


**Fig. 3. Relationship between membrane ion separation performance and molecular packing.** (**A**) Flux of NaCl, $MgCl_2$, and $Na_2SO_4$ across various membranes tested under 0.1 M single-salt conditions, accompanied by the corresponding selectivity of $Na^+/Mg^{2+}$ and $Cl^-/SO_4^{2-}$. (**B** and **C**) Projections of SAXS patterns for (**D**) COF-170 and (**E**) COF-976. (**F** and **G**) In-plane 2D grazing-incidence wide-angle x-ray scattering (GIWAXS) patterns for COF-170 and COF-976 membranes. (**H** and **I**) Out-of-plane 2D GIWAXS patterns for COF-170 and COF-976 membranes, respectively.

COF-170 was more sharply defined compared to that of COF-976. Using the Debye-Scherrer method, we calculated the average grain sizes of the COF-170 and COF-976 membranes as 23 and 19 nm, respectively, in the 2D plane. Furthermore, the 2D GIWAXS patterns of these membranes displayed distinct differences, underscoring variations in the stacking order of their 2D nanosheets. Such differences are presumed to be crucial in determining the disparate performance of the two membranes. Specifically, the GIWAXS pattern of COF-976 showed Bragg peaks in a ring pattern, suggesting a random orientation of the 2D layers (Fig. 3, F and G). Conversely, the COF-170 membrane exhibited pronounced in-plane Bragg diffraction, especially along the $Q_x$ axis, indicating an alignment of the hexagonal lattice of COF-170 grains parallel to the substrate surface. The π-π stacking order, determined according to the diffuse arc in the GIWAXS pattern, revealed that most grains in the COF-170 membrane align their *c* axes within about $\varnothing = 16°$ of the surface normal, which is notably smaller than the broader orientation of about 54° observed in the COF-976 membrane (Fig. 3, H and I) (*64*). The less orderly orientation in COF-976 is believed to arise from unoriented precipitates formed during the synthesis process, potentially obstructing the NaCl transport pathway. The study posits that the lamellar ordering of nanosheets in the COF-170 membrane enhances the permeation pathway for NaCl while blocking the leakage of $Na_2SO_4$, thereby improving the separation performance of the membrane. Using Herman's orientation function (Eq. 1), we quantified the lamellar ordering of the 2D COF sheets within the membranes and assessed NaCl transmembrane activity (*65*)

$$f = \frac{3\left(\cos^2 \emptyset\right) - 1}{2} \quad (1)$$

A value of $f = 1$ denotes perfect parallel alignment of COF grains to the support, whereas $f = 0$ indicates random orientation. The calculated *f* values for the COF-170 and COF-976 membranes are 0.89 and 0.02, respectively, indicating a direct correlation between NaCl flux (89.7 and 20.3 mmol $m^{-2}$ $hour^{-1}$ for the COF-170 and COF-976 membranes, respectively) and membrane lamellar ordering. The observed anomalous ion transport behavior is attributed to the distinct charge distribution resulting from oriented growth of COF-170, with a negatively charged exterior and a positively charged interior within the COF membrane. These electrostatic interactions, influenced by the size of aligning π systems, notably enhance rejection of multivalent ions like $Mg^{2+}$ and $SO_4^{2-}$ while exerting minimal influence on univalent symmetric salts like NaCl. As a result, COF-170 demonstrates higher NaCl flux compared to $MgCl_2$ and $Na_2SO_4$. Conversely, random packing of COF nanosheets introduces variability in charge distribution and weakens electrostatic interactions with ions. This random packing increases fluxes of $MgCl_2$ and $Na_2SO_4$, despite thicker membranes. The decreased flux of NaCl in COF-976 is attributed to longer mass transport pathways caused by random packing and greater membrane thickness. It is speculated that a membrane composed entirely of fully ordered 2D COF nanosheets could function as an ultra-permeable and super-selective ion sieve membrane, ideal for efficient separation processes.

## Using MD simulations for insight into the mechanisms of ion screening in membrane

To elucidate the ion-screening mechanism of the oriented COF membrane, molecular dynamics (MD) simulations were conducted to analyze ion behavior as it traverses the membrane (fig. S11). Separate simulations were performed for binary systems of NaCl and $Na_2SO_4$, as well as NaCl and $MgCl_2$, to distinguish between anions and cations with varying valences. Instantaneous configuration diagrams revealed a notable trend: $Cl^-$ ions exhibited a propensity to penetrate and traverse membrane pores more rapidly than $SO_4^{2-}$ ions (Fig. 4A and fig. S12). Further analysis of the number density distribution of $Na^+$, $Cl^-$, and $SO_4^{2-}$ ions over a simulation period from 24 to 26 ns unveiled a pronounced density peak of $SO_4^{2-}$ ions on the feed side of the COF membrane. Within the membrane itself, the number density of $SO_4^{2-}$ ions exceeded that of $Cl^-$ ions. However, on the permeation side, $Cl^-$ ions dominated, indicating their more efficient transmembrane traversal (Fig. 4B). This observation was supported by diffusion coefficients of $Cl^-$ and $SO_4^{2-}$, showing values of $8.15 \times 10^{-6}$ and $4.77 \times 10^{-6}$ $cm^2$ $s^{-1}$, respectively (Fig. 4C). 2D density maps depicted $Cl^-$ ions as broadly dispersed across the membrane, while $SO_4^{2-}$ ions tended to centralize, suggesting a stronger affinity toward the pore channels (Fig. 4D and fig. S13). The assessment of binding energy clarified these observed ion behaviors, with the binding energies of $SO_4^{2-}$ and $Cl^-$ ions toward the COF membrane segment calculated to be −2.88 and −0.69 kcal $mol^{-1}$, respectively (fig. S14). On the basis of these observations, it is concluded that the eclipsed stacked COF membrane exhibits a preference for retaining $SO_4^{2-}$ ions over $Cl^-$ ions. This selectivity is primarily attributed to two fundamental mechanisms. The first is interface retention, where $SO_4^{2-}$ ions encounter a more formidable energy barrier when attempting to penetrate the membrane. The second mechanism involves pore channel retention, where the binding energy of $SO_4^{2-}$ ions to the membrane exceeds that of $Cl^-$ ions, resulting in a more challenging passage for $SO_4^{2-}$ ions across the membrane. Moreover, MD simulations for $Na^+$ and $Mg^{2+}$ ions indicated that fewer $Mg^{2+}$ ions traversed the membrane compared to $Na^+$ ions within the same timeframe (Fig. 4E and figs. S15 to S17). This behavior stems from the membrane negatively charged exterior, which more strongly attracts higher-valent cations. In addition, the repelling force from the Donnan potential, which is created at the solution/membrane interface by the positively charged interior, increases with the valence of the co-ions (*66*–*68*). These factors effectively impede the passage of $Mg^{2+}$ ions through the pore channels more than $Na^+$ ions, thereby contributing to the observed selectivity between $Na^+$ and $Mg^{2+}$.

## Analyzing anion and cation screening capabilities in the oriented COF membrane

To gain deeper insights into ion transmembrane behavior, we conducted additional experiments using the highly efficient COF-170/PAN membrane. Initially, our focus was to determine the apparent transmembrane activation energies of various ions ($Na^+$, $Mg^{2+}$, $Cl^-$, and $SO_4^{2-}$) using an electric field-driven approach (fig. S18) (*69*). This method allowed for the separate evaluation of anions and cations (see details in the Supplementary Materials). By analyzing the Arrhenius plots, which depict ionic conductivity against temperature, we calculated the apparent activation energies ($E_a$) for these ions as they transport across the membrane. The results were $12.6 \pm 0.6$ kJ $mol^{-1}$ for $Na^+$, $26.4 \pm 1.2$ kJ $mol^{-1}$ for $Mg^{2+}$, $20.0 \pm 0.1$ kJ $mol^{-1}$ for $Cl^-$, and $27.5 \pm 0.8$ kJ $mol^{-1}$ for $SO_4^{2-}$ (Fig. 5A and fig. S19). Notably, each ion type consistently exhibited similar energy barriers across various salts, validating our electrochemical methodology in accurately measuring individual ion transport

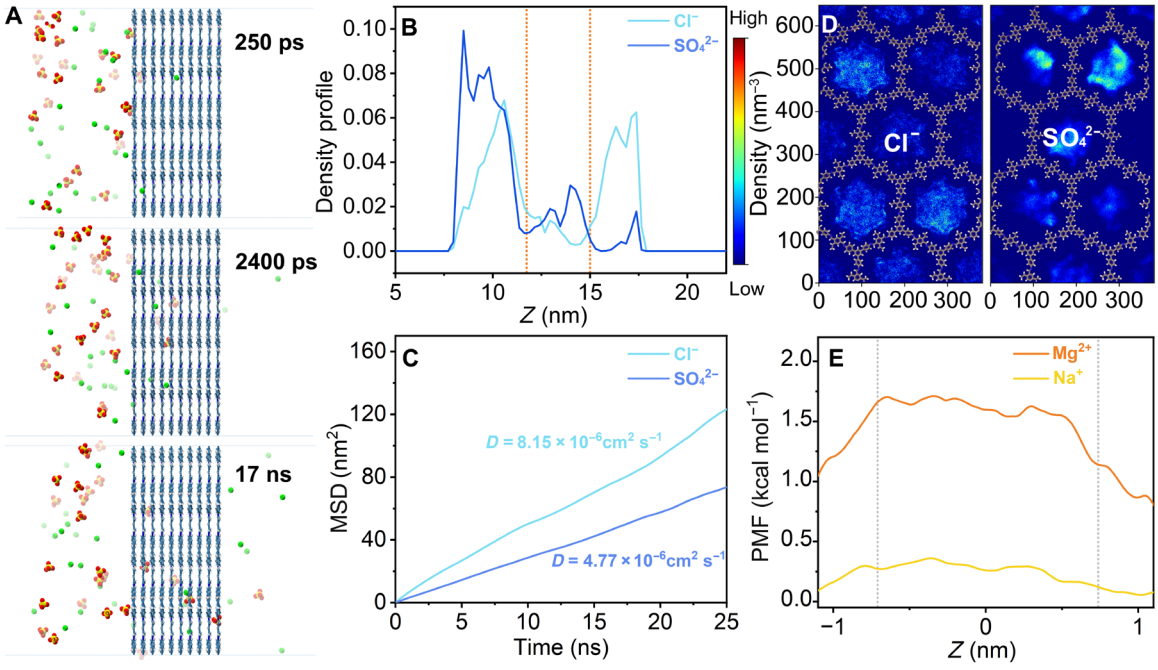


**Fig. 4. MD simulations.** (**A**) Simulation snapshots visually depict the transmembrane behavior of $Cl^-$ and $SO_4^{2-}$ ions (blue, COF layers; green, $Cl^-$; red and yellow, $SO_4^{2-}$). (**B**) Ion density profiles along the *z* axis in the COF are presented, with orange dashed lines indicating the membrane boundaries. (**C**) The diffusion coefficients of $Cl^-$ and $SO_4^{2-}$ ions across the COF membrane. MSD, mean square displacement. (**D**) A 2D density map showcases the distribution of $Cl^-$ and $SO_4^{2-}$ ions within the *xy* plane of the membrane. (**E**) Potentials of mean force (PMF) profiles for $Na^+$ and $Mg^{2+}$ ions across the COF membrane.

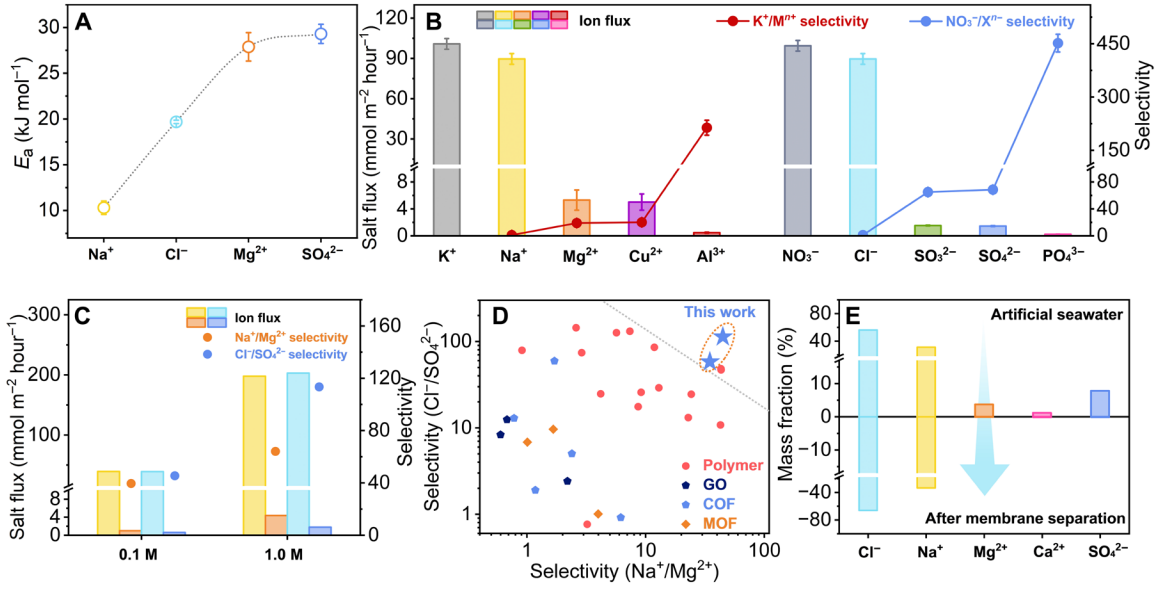


**Fig. 5. Evaluation of ion separation performance over COF-170/PAN.** (**A**) Apparent ion transmembrane activation energies across the COF-170/PAN membrane. (**B**) Ion flux and relative ion selectivities across the COF-170/PAN membrane tested under single-salt conditions at a concentration of 0.1 M for each salt. (**C**) Performance of the COF-170/PAN membrane in ternary-salt mixtures, showing ion flux and selectivity metrics under conditions with equimolar concentrations of NaCl, $Na_2SO_4$, and $MgCl_2$, measured over a test duration of 30 min. (**D**) Comparison of the ion selectivity of COF-170/PAN with reported systems. (**E**) Ion composition of artificial seawater before and after membrane separation, assessed over a testing period of 3 hours.

energy barriers. Our findings indicate that the energy required for ions to traverse the membrane is primarily influenced by their charge; higher valence ions necessitate more energy due to enhanced ion-π interactions. Notably, the apparent activation energy for $Na^+$ transport across the COF-170/PAN membrane is lower than its intrinsic activation energy for diffusion in water (*70*). This suggests that the COF-170/PAN membrane offers minimal resistance to $Na^+$ transport, an efficiency attributed to its unique ESP distribution. Similarly, membranes equipped with selective binding sites have been observed to lower the energy barriers for ion transmembrane transport (*71*). To corroborate this, we measured the transmembrane fluxes of various salts (KCl, $NaNO_3$, $CuCl_2$, $Na_2SO_3$, $AlCl_3$, and $Na_3PO_4$) in 0.1 M single-salt conditions. The outcomes reinforced our hypothesis, showing a distinct relationship between ion charge and permeation rates. Specifically, the triply charged anion $PO_4^{3-}$ had lower flux compared to the singly charged $NO_3^-$ and $Cl^-$ and the divalent $SO_4^{2-}$ and $SO_3^{2-}$. This resulted in selectivities of 451 for $NO_3^-/PO_4^{3-}$, 407 for $Cl^-/PO_4^{3-}$, 6.6 for $SO_4^{2-}/PO_4^{3-}$, and 7.0 for $SO_3^{2-}/PO_4^{3-}$. In a similar pattern, the triply charged cation $Al^{3+}$ demonstrated considerably lower flux than the singly charged $K^+$ and $Na^+$ and the divalent $Mg^{2+}$ and $Cu^{2+}$, resulting in ratios of 214, 190, 11, and 12 for $K^+/Al^{3+}$, $Na^+/Al^{3+}$, $Mg^{2+}/Al^{3+}$, and $Cu^{2+}/Al^{3+}$, respectively (Fig. 5B). For ions with identical valences, such as $K^+/Na^+$, $Cl^-/NO_3^-$, and $SO_4^{2-}/SO_3^{2-}$, we observed nearly equal fluxes with ratios of 1.1, 0.9, and 0.95, respectively. Because the pore size of our membrane greatly exceeds that of hydrated ions, the observed differences in transmembrane flux of ions with the same valence mainly arise from variations in their intrinsic diffusion coefficients (*72*).

Subsequently, we investigated the impact of varying salt concentrations on membrane separation performance. Our results demonstrated a consistent increase in flux for all salts as their concentrations rose. Notably, there was a concentration-dependent enhancement in selectivity for mono- and divalent anions (figs. S20 and S21). Specifically, the selectivity of $NO_3^-$ over $SO_4^{2-}$ substantially increased from 67 to 118, and that of $Cl^-$ over $SO_4^{2-}$ rose from 63 to 81 when the concentration changed from 0.05 to 1 M. However, the selectivity trends for cations exhibited a more intricate pattern. For $Na^+$ over $Mg^{2+}$, selectivity initially rose from 17 to 21 as the concentration increased from 0.05 to 0.5 M but then returned to 17 at a 1 M concentration. Similarly, for $K^+$ over $Mg^{2+}$, selectivity improved from 18 to 24 with a concentration increase from 0.05 to 0.5 M but decreased to 19 upon further increasing the concentration to 1 M. The fluctuations in cation selectivity across different concentrations, coupled with the proportional increase in selectivity for monovalent anions compared to divalent anions, led us to the following rationale: For the $Cl^-$ over $SO_4^{2-}$ selectivity, the enhancement is primarily due to the negatively charged membrane surface, which impedes the approach of $SO_4^{2-}$ ions. As a result, $SO_4^{2-}$ ions tend to aggregate in the feed solution due to this obstruction, with aggregation becoming more pronounced as concentration increases, while $Cl^-$ ions remain unaffected. MD simulations corroborate these findings, highlighting a notable increase in $Cl^-$ ions passing through the membrane compared to $SO_4^{2-}$, thereby enhancing the $Cl^-/SO_4^{2-}$ selectivity as salt concentration rises (fig. S22). Regarding cation selectivity, the separation ratio for monovalent over divalent cations initially increases and then declines with higher salt concentrations. This trend is attributed to strong cation-π interactions between $Mg^{2+}$ ions and the membrane, especially at lower concentrations, which produce a positive surface potential. This potential impedes the entry of $Mg^{2+}$ into the membrane pores, with the repulsive force increasing as more $Mg^{2+}$ ions accumulate. However, monovalent $Na^+$ and $K^+$ ions, which exhibit weaker cation-π interactions, face less resistance from the membrane, thus enhancing their selectivity over $Mg^{2+}$ as salt concentration increases. Nevertheless, at higher concentrations of $MgCl_2$, interactions among $Mg^{2+}$ ions dominate, leading to ion-ion interactions that diminish their interaction with the membrane, thereby reducing membrane selectivity (*73*). This behavior is corroborated by MD simulations, which reveal a decrease in $Mg^{2+}$ ions near the membrane surface as solution concentration increases. Specifically, within a 0.9 nm distance from the membrane, $Mg^{2+}$ ions account for 18% of the total $Mg^{2+}$ count in a 0.1 M $MgCl_2$ solution but only 12% in a 1 M solution. Meanwhile, the surface concentration of $Na^+$ ions remains relatively stable across changes in NaCl concentration, fluctuating slightly between 11 and 10%.

To evaluate the separation performance of the COF-170/PAN membrane amidst competing ions, diffusion experiments were carried out using binary feed solutions, which contained equal molar concentrations of $Na^+/K^+$ with $Mg^{2+}$ and $NO_3^-/Cl^-$ with $SO_4^{2-}$, at concentrations ranging from 0.05 to 1 M (figs. S23 to S26). The findings indicated a general increase in separation efficiency for both mono- and divalent cations and anions as salt concentration escalated, except for the $NO_3^-/SO_4^{2-}$ pair, which saw a decline in efficiency as ion concentrations increased. The highest selectivity values recorded were 30 for $Na^+/Mg^{2+}$, 97 for $K^+/Mg^{2+}$, 47 for $Cl^-/SO_4^{2-}$, and 69 for $NO_3^-/SO_4^{2-}$. Notably, improved selectivity was observed for mono- and divalent cations in binary conditions compared to single-salt scenarios. However, the separation factor for mono-/divalent anions in binary-salt conditions consistently remained lower than that in single-salt conditions. These phenomena can be rationalized as follows: Cation-π interactions between $Na^+/K^+$ ions and the membrane promoted closer proximity of these ions to the membrane surface, thereby diminishing the adsorption of $Mg^{2+}$ ions due to competitive interactions in binary conditions (*74*, *75*). In addition, because the electrostatic interaction between monovalent $Na^+$ ions and the membrane is weaker, $Na^+$ ions were more readily transported across the membrane under concentration gradients, thereby enhancing the separation ratio of monovalent to divalent cations in binary-salt conditions compared to single-salt scenarios. In contrast, competitive adsorption, where less strongly bound $Cl^-$ ions preempt the channel surfaces, impeded $SO_4^{2-}$ binding with the positively charged channel surface, as supported by theoretical simulations (*76*, *77*), thus increasing the transmembrane activity of $SO_4^{2-}$ and showing decreased selectivity.

Encouraged by these results, we proceeded to assess the performance of the COF-170 membrane in concurrently distinguishing monovalent cations and anions from their multivalent counterparts. Given the prevalence of ions such as $Na^+$, $Mg^{2+}$, $Cl^-$, and $SO_4^{2-}$ in natural water sources, we evaluated the ion separation capabilities of the COF-170/PAN membrane under ternary-salt conditions using NaCl, $Na_2SO_4$, and $MgCl_2$. The COF-170/PAN membrane exhibited impressive selectivity, with values of 64 for $Cl^-/SO_4^{2-}$ and 39 for $Na^+/Mg^{2+}$ at a concentration of 0.1 M for each salt. Intriguingly, at a higher salt concentration of 1 M, the selectivity of the membrane improved, reaching 113 for $Cl^-/SO_4^{2-}$ and 45 for $Na^+/Mg^{2+}$, positioning it among the top-performing systems reported (Fig. 5, C and D, fig. S27, and table S2). Particularly in ternary-salt conditions, there is a noted enhancement in the separation of cations and anions of different valences. This improvement is attributed to strong cation-π interactions between $Mg^{2+}$ ions

and the membrane, which form a positively charged layer that preferentially binds and retains higher valent $SO_4^{2-}$ ions, reducing their flux. This mechanism is supported by the observed density distribution of $Na^+$, $Cl^-$, $Mg^{2+}$, and $SO_4^{2-}$ ions, which shows a pronounced peak for $Mg^{2+}$ and $SO_4^{2-}$ at the feed side of the COF membrane (fig. S28). Consequently, the relatively weaker electrostatic interactions affecting $Na^+$ and $Cl^-$, compared to those involving $Mg^{2+}$ and $SO_4^{2-}$, enhance the selectivity for $Na^+/Mg^{2+}$ and $Cl^-/SO_4^{2-}$ in ternary-salt conditions over single-salt and binary-salt conditions.

It is important to highlight that membranes carrying either negative or positive charges generally exhibit reduced retention as concentration increases, attributed to the diminishing Donnan exclusion effects with elevated feed electrolyte concentrations. Typically, an increase in ionic strength shields the membrane charge, reducing its effective charge and, consequently, its retention capacity (*78*). Contrarily, our results reveal an unusual behavior in COF-170, characterized by a negatively charged exterior and a positively charged interior. In our experiments, selectivity increases with salt concentration in both binary and ternary systems. MD simulations support these findings, indicating that the permeation ratios of $Na^+/K^+$ over $Mg^{2+}$ and $Cl^-$ over $SO_4^{2-}$ ions across the COF membrane increase with rising salt concentration (fig. S29). In scenarios involving $SO_4^{2-}$, both in binary and ternary systems, there is notable aggregation of $SO_4^{2-}$ ions, or of $SO_4^{2-}$ and $Mg^{2+}$ ions, on the feed side due to strong ion-ion interactions. This aggregation becomes more pronounced as salt concentration increases (fig. S30). Consequently, fewer of these ions penetrate the membrane pores compared to monovalent ions, thereby augmenting selective transport across the membrane. In addition, the rise in salt concentration exacerbates competitive interactions between the membrane and the ions $Na^+$ and $Mg^{2+}$, thus enhancing the separation efficiency of binary cations. These nuanced findings underscore the complex interplay between salt types and concentrations and their effects on membrane selectivity.

We extended our investigation into the performance of COF-170/PAN under electrically driven conditions by applying a constant voltage of −1 V. This voltage was applied to enhance ion flux, thereby improving the separation efficiency (*79*). To minimize the impact of concentration gradients on ion transport, a ternary solution with equal concentrations (0.1 M) of NaCl, $Na_2SO_4$, and $MgCl_2$ was used. Despite a sixfold increase in ion flux, the selectivity ratios for $NaCl/Na_2SO_4$ and $NaCl/MgCl_2$ remained well preserved at 58 and 35 (Fig. 5D, fig. S27, and table S2). A notable finding from our study is the remarkable stability of the membrane in ion separation applications. This stability was evident through consistent selectivity and flux observed during continuous operation over 3 hours and across at least 10 reuse cycles (fig. S31). Furthermore, the composition, crystallinity, and morphology of the COF-170 membrane remained consistent throughout the recycling process, underscoring its suitability for prolonged usage and durability in real-world applications (figs. S32 to S35).

To showcase the proof-of-concept applicability of the COF-170/PAN membrane, we assessed its capability to extract NaCl from seawater, a procedure of considerable importance given the widespread industrial and everyday usage of high-quality NaCl. Conventional NaCl production methods often involve straightforward crystallization, a method that commonly suffers from contamination with undesired impurities such as $Mg^{2+}$, $Ca^{2+}$, and $SO_4^{2-}$ ions. Such impurities typically require chemical treatments for their precipitation (*80*–*83*). What distinguishes the COF-170/PAN membrane is its exceptional permeability to NaCl while efficiently impeding the passage of divalent ions. Throughout the 3-hour electro-driven ion separation process, the combined mass fraction of $Na^+$ and $Cl^-$ notably increases to 99.57% from a starting seawater content of 87.32%, with a flux of 169 mmol $m^{-2}$ $hour^{-1}$. Meanwhile, the total mass fraction of $Mg^{2+}$, $Ca^{2+}$, and $SO_4^{2-}$ ions reduces to a minimal 0.43% from 12.68% (Fig. 5E and table S3). Under identical conditions, a reverse osmosis membrane (LCLE-4040 from Dow Corp.) achieved a NaCl mass fraction of 92.9% and a flux of 5.21 mmol $m^{-2}$ $hour^{-1}$, thereby highlighting the efficiency of COF-170/PAN. Furthermore, the operational stability of the COF-170/PAN membrane is noteworthy, maintaining consistent ion separation ratios even after 15 continuous hours of operation (fig. S36). In addition, the separation efficiency of COF-170/PAN can be readily restored with a simple rinsing with water, thereby enhancing its practicality and effectiveness. This characteristic makes the COF-170/PAN membrane not only efficient in its primary function but also operationally robust and easily maintainable, bolstering its appeal for real-world applications.

## DISCUSSION

In summary, this work presents an alternative strategy to tackle the intricate challenge of designing membrane materials with the capability to simultaneously filter both cations and anions. Our research underscores the viability of attaining this dual functionality by strategically engineering the molecular packing within transport channels, obviating the necessity for specific functional modifications. The extensive face-to-face π-π stacking within the orientated 2D COF membrane enhances ion-π interactions between leading to remarkable selectivity. This work not only establishes a solid foundation for advancing ion separation membrane materials but also introduces innovative perspectives on selectively extracting specific components from intricate mixtures. Looking forward, through the continued optimization of membrane orientation and composition, these synthetically engineered membranes demonstrate substantial potential, not only to rival but also to potentially surpass the separation efficacy exhibited by their natural biological counterparts.

## MATERIALS AND METHODS

The commercially available reagents were purchased in high purity and used without purification. The PAN ultrafiltration membrane, with a molecular weight cutoff of 50,000 Da, was purchased from Sepro Membranes Inc. (Carlsbad, CA, USA). PXRD patterns were collected using a Bruker AXS D8 Advance A25 powder x-ray diffractometer (40 kV, 40 mA) using Cu Kα (λ = 1.5406 Å) radiation. SEM was performed on a Hitachi SU 8000 instrument. The thickness of the COF membrane onto the Si wafers was analyzed using an atomic force microscope (NanoScope, Veeco) in air at 25°C. For high-resolution transmission electron microscope, a JEM-2100F was used. Gas adsorption isotherms were measured using a surface area analyzer ASAP 2020. The $N_2$ sorption isotherms were recorded at 77 K, using a liquid $N_2$ bath. FTIR spectra were recorded on a Nicolet Impact 410 FTIR spectrometer. $^{13}C$ (100.5 MHz) cross-polarization magic-angle spinning was recorded on a Varian infinity plus 400 spectrometer equipped with a magic-angle spin probe in a 4-mm $ZrO_2$ rotor. The GIWAXS measurements were performed at BL14B1 beamline of the Shanghai Synchrotron Radiation Facility. Si

wafers served as the substrate for all samples. Achieving high-resolution in-depth imaging, an x-ray with a wavelength of 1.238 Å was used for incident-angle–dependent measurements, with the incident angle fixed at 0.2°. Membrane samples, cut into small pieces (1 cm by 1 cm), were affixed to silicon wafers. SAXS experiments were performed using the XEUSS 3.0* instrument. The x-ray wavelength used was 0.135 nm, and the distance between the sample and detector was set at 100 mm.

## Supplementary Materials

**This PDF file includes:**

Supplementary Text
Figs. S1 to S36
Tables S1 to S3
References

## REFERENCES AND NOTES


1. R. Epsztein, R. M. DuChanois, C. L. Ritt, A. Noy, M. Elimelech, Towards single-species selectivity of membranes with subnanometre pores. *Nat. Nanotechnol.* **15**, 426–436 (2020).
2. S. Kandambeth, B. P. Biswal, H. D. Chaudhari, K. C. Rout, S. K. H., S. Mitra, S. Karak, A. Das, R. Mukherjee, U. K. Kharul, R. Banerjee, Selective molecular sieving in self-standing porous covalent-organic-framework membranes. *Adv. Mater.* **29**, 1603945 (2017).
3. J. Wang, Z. Cui, S. Li, Z. Song, M. He, D. Huang, Y. Feng, Y. Liu, K. Zhou, X. Wang, L. Wang, Unlocking osmotic energy harvesting potential in challenging real-world hypersaline environments through vermiculite-based hetero-nanochannels. *Nat. Commun.* **15**, 608 (2024).
4. P. Zuo, C. Ye, Z. Jiao, J. Luo, J. Fang, U. S. Schubert, N. B. McKeown, T. L. Liu, Z. Yang, T. Xu, Near-frictionless ion transport within triazine framework membranes. *Nature* **617**, 299–305 (2023).
5. L. Chen, G. Shi, J. Shen, B. Peng, B. Zhang, Y. Wang, F. Bian, J. Wang, D. Li, Z. Qian, G. Xu, G. Liu, J. Zeng, L. Zhang, Y. Yang, G. Zhou, M. Wu, W. Jin, J. Li, H. Fang, Ion sieving in graphene oxide membranes via cationic control of interlayer spacing. *Nature* **550**, 380–383 (2017).
6. L. Cao, X. He, Z. Jiang, X. Li, Y. Li, Y. Ren, L. Yang, H. Wu, Channel-facilitated molecule and ion transport across polymer composite membranes. *Chem. Soc. Rev.* **46**, 6725–6745 (2017).
7. Z. Lu, Y. Wu, L. Ding, Y. Wei, H. Wang, A lamellar MXene ($Ti_3C_2T_x$)/PSS composite membrane for fast and selective lithium-ion separation. *Angew. Chem. Int. Ed. Engl.* **60**, 22265–22269 (2021).
8. A. Iddya, P. Zarzycki, R. Kingsbury, C. M. Khor, S. Ma, J. Wang, I. Wheeldon, Z. J. Ren, E. M. V. Hoek, D. Jassby, A reverse-selective ion exchange membrane for the selective transport of phosphates via an outer-sphere complexation-diffusion pathway. *Nat. Nanotechnol.* **17**, 1222–1228 (2022).
9. R. Tan, A. Wang, R. Malpass-Evans, R. Williams, E. W. Zhao, T. Liu, C. Ye, X. Zhou, B. P. Darwich, Z. Fan, L. Turcani, E. Jackson, L. Chen, S. Y. Chong, T. Li, K. E. Jelfs, A. I. Cooper, N. P. Brandon, C. P. Grey, N. B. McKeown, Q. Song, Hydrophilic microporous membranes for selective ion separation and flow-battery energy storage. *Nat. Mater.* **19**, 195–202 (2020).
10. W. Xian, X. Zuo, C. Zhu, Q. Guo, Q.-W. Meng, X. Zhu, S. Wang, S. Ma, Q. Sun, Anomalous thermo-osmotic conversion performance of ionic covalent-organic-framework membranes in response to charge variations. *Nat. Commun.* **13**, 3386 (2022).
11. R. M. DuChanois, M. Heiranian, J. Yang, C. J. Porter, Q. Li, X. Zhang, R. Verduzco, M. Elimelech, Designing polymeric membranes with coordination chemistry for high-precision ion separations. *Sci. Adv.* **8**, eabm9436 (2022).
12. M. Zhang, P. Zhao, P. Li, Y. Ji, G. Liu, W. Jin, Designing biomimic two-dimensional ionic transport channels for efficient ion sieving. *ACS Nano* **15**, 5209–5220 (2021).
13. Z. Zhang, X. Huang, Y. Qian, W. Chen, L. Wen, L. Jiang, Engineering smart nanofluidic systems for artificial ion channels and ion pumps: From single-pore to multichannel membranes. *Adv. Mater.* **32**, 1904351 (2020).
14. Q.-W. Meng, S. Wu, M. Liu, Q. Guo, W. Xian, X. Zuo, S. Wang, H. Yin, S. Ma, Q. Sun, Guanidinium-based covalent organic framework membrane for single-acid recovery. *Sci. Adv.* **9**, eadh0207 (2023).
15. B. Shi, X. Pang, B. Lyu, H. Wu, J. Shen, J. Guan, X. Wang, C. Fan, L. Cao, T. Zhu, Y. Kong, Y. Liu, Z. Jiang, Spacer-engineered ionic channels in covalent organic framework membranes toward ultrafast proton transport. *Adv. Mater.* **35**, 2211004 (2023).
16. L. Wang, Y. Wang, Z. Li, T. Li, R. Zhang, J. Li, B. Liu, Z. Lv, W. Cai, S. Sun, W. Hu, Y. Lu, G. Zhu, PAF-6 doped with phosphoric acid through alkaline nitrogen atoms boosting high-temperature proton-exchange membranes for high performance of fuel cells. *Adv. Mater.* **35**, 2303535 (2023).
17. M. Zhang, K. Guan, Y. Ji, G. Liu, W. Jin, N. Xu, Controllable ion transport by surface-charged graphene oxide membrane. *Nat. Commun.* **10**, 1253 (2019).
18. Z. Tan, S. Chen, X. Peng, L. Zhang, C. Gao, Polyamide membranes with nanoscale turing structures for water purification. *Science* **360**, 518–521 (2018).
19. J. Li, H. Peng, K. Liu, Q. Zhao, Polyester nanofiltration membranes for efficient cations separation. *Adv. Mater.* **36**, 2309406 (2024).
20. G. Zhao, H. Gao, Z. Qu, H. Fan, H. Meng, Anhydrous interfacial polymerization of sub-1 Å sieving polyamide membrane. *Nat. Commun.* **14**, 7624 (2023).
21. L. Hou, W. Xian, S. Bing, Y. Song, Q. Sun, L. Zhang, S. Ma, Understanding the ion transport behavior across nanofluidic membranes in response to the charge variations. *Adv. Funct. Mater.* **31**, 2009970 (2021).
22. Y. Han, Y. Wang, M. Wang, H. Dong, Y. Nie, S. Zhang, H. He, Nanofluid-guided janus membrane for high-efficiency electricity generation from water evaporation. *Adv. Mater.* **36**, 2312209 (2024).
23. Y. Li, Z. Pei, D. Luan, X. W. D. Lou, Triple-phase photocatalytic $H_2O_2$ production on a Janus fiber membrane with asymmetric hydrophobicity. *J. Am. Chem. Soc.* **146**, 3343–3351 (2024).
24. H.-C. Yang, Y. Xie, J. Hou, A. K. Cheetham, V. Chen, S. B. Darling, Janus membranes: Creating asymmetry for energy efficiency. *Adv. Mater.* **30**, 1801495 (2018).
25. L. Zheng, N. Liu, Y. Liu, N. Li, J. Zhang, C. Wang, W. Zhu, Y. Chen, D. Ying, J. Xu, Z. Yang, X. Gao, J. Tang, X. Wang, Z. Liang, R. Zou, Y. Li, P. Gao, X. Wei, H.-W. Wang, H. Peng, Atomically thin bilayer Janus membranes for cryo-electron microscopy. *ACS Nano* **15**, 16562–16571 (2021).
26. H.-C. Yang, J. Hou, V. Chen, Z.-K. Xu, Janus membranes: Exploring duality for advanced separation. *Angew. Chem. Int. Ed. Engl.* **55**, 13398–13407 (2016).
27. D. Shi, T. Gong, R. Wang, W. Qing, S. Shao, Control the hydrophilic layer thickness of Janus membranes by manipulating membrane wetting in membrane distillation. *Water Res.* **237**, 119984 (2023).
28. X. Qiang, S. Franzka, G. Quintieri, X. Dai, C. K. Wong, A. H. Gröschel, Size-controlled formation of polymer Janus discs. *Angew. Chem. Int. Ed. Engl.* **60**, 21668–21672 (2021).
29. H. Zeng, P. Liu, G. Feng, F. Huang, π-Metalated [$1_5$]paracyclophanes: Synthesis and binding to oxo-anions via anion-π interactions. *J. Am. Chem. Soc.* **141**, 16501–16511 (2019).
30. D. Bai, T. Yan, S. Wang, Y. Wang, J. Fu, X. Fang, J. Zhu, J. Liu, Reversible ligand-gated ion channel via interconversion between hollow single helix and intertwined double helix. *Angew. Chem. Int. Ed. Engl.* **59**, 13602–13607 (2020).
31. F. Chen, J. Shen, N. Li, A. Roy, R. Ye, C. Ren, H. Zeng, Pyridine/oxadiazole-based helical foldamer ion channels with exceptionally high $K^+/Na^+$ selectivity. *Angew. Chem. Int. Ed. Engl.* **59**, 1440–1444 (2020).
32. S.-P. Zheng, L.-B. Huang, Z. Sun, M. Barboiu, Self-assembled artificial ion-channels toward natural selection of functions. *Angew. Chem. Int. Ed. Engl.* **60**, 566–597 (2021).
33. A. Dhotel, Z. Chen, L. Delbreilh, B. Youssef, J.-M. Saiter, L. Tan, Molecular motions in functional self-assembled nanostructures. *Int. J. Mol. Sci.* **14**, 2303–2333 (2013).
34. A.-B. Bornhof, A. Bauzá, A. Aster, M. Pupier, A. Frontera, E. Vauthey, N. Sakai, S. Matile, Synergistic anion-$(\pi)_n$-π catalysis on π-stacked foldamers. *J. Am. Chem. Soc.* **140**, 4884–4892 (2018).
35. D.-X. Wang, M.-X. Wang, Exploring anion-π interactions and their applications in supramolecular chemistry. *Acc. Chem. Res.* **53**, 1364–1380 (2020).
36. G. Zhao, H. Zhu, Cation-π interactions in graphene-containing systems for water treatment and beyond. *Adv. Mater.* **32**, 1905756 (2020).
37. E. A. Meyer, R. K. Castellano, F. Diederich, Interactions with aromatic rings in chemical and biological recognition. *Angew. Chem. Int. Ed. Engl.* **42**, 1210–1250 (2003).
38. B. Gong, Z. Shao, Self-assembling organic nanotubes with precisely defined, sub-nanometer pores: Formation and mass transport characteristics. *Acc. Chem. Res.* **46**, 2856–2866 (2013).
39. H. Zuo, B. Lyu, J. Yao, W. Long, Y. Shi, X. Li, H. Hu, A. Thomas, J. Yuan, B. Hou, W. Zhang, Y. Liao, Bioinspired gradient covalent organic framework membranes for ultrafast and asymmetric solvent transport. *Adv. Mater.* **36**, 2305755 (2024).
40. L. Sun, Z. Li, L. Zhai, H. Moon, C. Song, K.-S. Oh, X. Kong, D. Han, Z. Zhu, Y. Wu, S.-Y. Lee, L. Mi, Electrostatic polarity-regulated, vinylene-linked cationic covalent organic frameworks as an ionic sieve membrane for long-cyclable lithium-sulfur batteries. *Energy Storage Mater.* **66**, 103222 (2024).
41. K. Wang, H. Yang, Z. Liao, S. Li, M. Hambsch, G. Fu, S. C. B. Mannsfeld, Q. Sun, T. Zhang, Monolayer-assisted surface-initiated schiff-base-mediated aldol polycondensation for the synthesis of crystalline $sp^2$ carbon-conjugated covalent organic framework thin films. *J. Am. Chem. Soc.* **145**, 5203–5210 (2023).

42. T. Mao, Z. Liu, X. Guo, Z. Wang, J. Liu, T. Wang, S. Geng, Y. Chen, P. Cheng, Z. Zhang, Engineering covalent organic frameworks with polyethylene glycol as self-sustained humidity-responsive actuators. *Angew. Chem. Int. Ed. Engl.* **62**, e202216318 (2023).
43. M. Wang, P. Zhang, X. Liang, J. Zhao, Y. Liu, Y. Cao, H. Wang, Y. Chen, Z. Zhang, F. Pan, Z. Zhang, Z. Jiang, Ultrafast seawater desalination with covalent organic framework membranes. *Nat. Sustain.* **5**, 518–526 (2022).
44. S. Zhao, C. Jiang, J. Fan, S. Hong, P. Mei, R. Yao, Y. Liu, S. Zhang, H. Li, H. Zhang, C. Sun, Z. Guo, P. Shao, Y. Zhu, J. Zhang, L. Guo, Y. Ma, J. Zhang, X. Feng, F. Wang, H. Wu, B. Wang, Hydrophilicity gradient in covalent organic frameworks for membrane distillation. *Nat. Mater.* **20**, 1551–1558 (2021).
45. Z. Guo, H. Wu, Y. Chen, S. Zhu, H. Jiang, S. Song, Y. Ren, Y. Wang, X. Liang, G. He, Y. Li, Z. Jiang, Missing-linker defects in covalent organic framework membranes for efficient $CO_2$ separation. *Angew. Chem. Int. Ed. Engl.* **61**, e202210466 (2022).
46. J. Du, Q. Sun, W. He, L. Liu, Z. Song, A. Yao, J. Ma, D. Cao, S. U. Hassan, J. Guan, J. Liu, A 2D soft covalent organic framework membrane prepared via a molecular bridge. *Adv. Mater.* **35**, 2300975 (2023).
47. A. Puthukkudi, S. Nath, P. Shee, A. Dutta, C. V. Rajput, S. Bommakanti, J. Mohapatra, M. Samal, S. Anwar, S. Pal, B. P. Biswal, Terahertz conductivity of free-standing 3D covalent organic framework membranes fabricated via triple-layer-dual interfacial approach. *Adv. Mater.* **36**, 2312960 (2024).
48. T. Liu, Y. Zhang, Z. Shan, M. Wu, B. Li, H. Sun, G. Su, R. Wang, G. Zhang, Covalent organic framework membrane for efficient removal of emerging trace organic contaminants from water. *Nat. Water* **1**, 1059–1067 (2023).
49. M. B. Asif, S. Kim, T. S. Nguyen, J. Mahmood, C. T. Yavuz, Covalent organic framework membranes and water treatment. *J. Am. Chem. Soc.* **146**, 3567–3584 (2024).
50. A. Knebel, J. Caro, Metal-organic frameworks and covalent organic frameworks as disruptive membrane materials for energy-efficient gas separation. *Nat. Nanotechnol.* **17**, 911–923 (2022).
51. X. Guo, T. Mao, Z. Wang, P. Cheng, Y. Chen, S. Ma, Z. Zhang, Fabrication of photoresponsive crystalline artificial muscles based on PEGylated covalent organic framework membranes. *ACS Cent. Sci.* **6**, 787–794 (2020).
52. H. Yang, J. Xu, H. Cao, J. Wu, D. Zhao, Recovery of homogeneous photocatalysts by covalent organic framework membranes. *Nat. Commun.* **14**, 2726 (2023).
53. L. Cao, I.-C. Chen, C. Chen, D. B. Shinde, X. Liu, Z. Li, Z. Zhou, Y. Zhang, Y. Han, Z. Lai, Giant osmotic energy conversion through vertical-aligned ion-permselective nanochannels in covalent organic framework membranes. *J. Am. Chem. Soc.* **144**, 12400–12409 (2022).
54. J. Ding, X. Guan, J. Lv, X. Chen, Y. Zhang, H. Li, D. Zhang, S. Qiu, H.-L. Jiang, Q. Fang, Three-dimensional covalent organic frameworks with ultra-large pores for highly efficient photocatalysis. *J. Am. Chem. Soc.* **145**, 3248–3254 (2023).
55. C. Yin, M. Liu, Z. Zhang, M. Wei, X. Shi, Y. Zhang, J. Wang, Y. Wang, Perpendicular alignment of covalent organic framework (COF) pore channels by solvent vapor annealing. *J. Am. Chem. Soc.* **145**, 11431–11439 (2023).
56. H. L. Nguyen, C. Gropp, Y. Ma, C. Zhu, O. M. Yaghi, 3d covalent organic frameworks selectively crystallized through conformational design. *J. Am. Chem. Soc.* **142**, 20335–20339 (2020).
57. Y. Zhang, C. Xing, Z. Mu, Z. Niu, X. Feng, Y. Zhang, B. Wang, Harnessing self-repairing and crystallization processes for effective enzyme encapsulation in covalent organic frameworks. *J. Am. Chem. Soc.* **145**, 13469–13475 (2023).
58. Q. Zhang, S. Dong, P. Shao, Y. Zhu, Z. Mu, D. Sheng, T. Zhang, X. Jiang, R. Shao, Z. Ren, J. Xie, X. Feng, B. Wang, Covalent organic framework-based porous ionomers for high-performance fuel cells. *Science* **378**, 181–186 (2022).
59. J. Li, L. Liu, X. Tang, X. Bai, Y. Liu, D. Wang, S. Tao, R. Liu, D. Jiang, Covalent organic frameworks: Reversible 3D coalesce via interlocked skeleton-pore actions and impacts on π electronic structures. *J. Am. Chem. Soc.* **145**, 26383–26392 (2023).
60. D. W. Burke, C. Sun, I. Castano, N. C. Flanders, A. M. Evans, E. Vitaku, D. C. McLeod, R. H. Lambeth, L. X. Chen, N. C. Gianneschi, W. R. Dichtel, Acid exfoliation of imine-linked covalent organic frameworks enables solution processing into crystalline thin films. *Angew. Chem. Int. Ed. Engl.* **59**, 5165–5171 (2020).
61. H. Sahabudeen, H. Qi, M. Ballabio, M. Položij, S. Olthof, R. Shivhare, Y. Jing, S. Park, K. Liu, T. Zhang, J. Ma, B. Rellinghaus, S. Mannsfeld, T. Heine, M. Bonn, E. Cánovas, Z. Zheng, U. Kaiser, R. Dong, X. Feng, Highly crystalline and semiconducting imine-based two-dimensional polymers enabled by interfacial synthesis. *Angew. Chem. Int. Ed. Engl.* **59**, 6028–6036 (2020).
62. F. Huang, Y. Wang, X. Dong, X. Lang, Imine-linked 2D covalent organic frameworks based on benzotrithiophene for visible-light-driven selective aerobic sulfoxidation. *J. Mater. Chem. A* **12**, 7036–7046 (2024).
63. Q. Sun, B. Aguila, J. Perman, L. D. Earl, C. W. Abney, Y. Cheng, H. Wei, N. Nguyen, L. Wojtas, S. Ma, Postsynthetically modified covalent organic frameworks for efficient and effective mercury removal. *J. Am. Chem. Soc.* **139**, 2786–2793 (2017).
64. J. W. Colson, A. R. Woll, A. Mukherjee, M. P. Levendorf, E. L. Spitler, V. B. Shields, M. G. Spencer, J. Park, W. R. Dichtel, Oriented 2D covalent organic framework thin films on single-layer graphene. *Science* **332**, 228–231 (2011).
65. T. Kongkhlang, K. Tashiro, M. Kotaki, S. Chirachanchai, Electrospinning as a new technique to control the crystal morphology and molecular orientation of polyoxymethylene nanofibers. *J. Am. Chem. Soc.* **130**, 15460–15466 (2008).
66. P. A. Gokturk, R. Sujanani, J. Qian, Y. Wang, L. E. Katz, B. D. Freeman, E. J. Crumlin, The Donnan potential revealed. *Nat. Commun.* **13**, 5880 (2022).
67. B.-B. Guo, C. Liu, C.-Y. Zhu, J.-H. Xin, C. Zhang, H.-C. Yang, Z.-K. Xu, Double charge flips of polyamide membrane by ionic liquid-decoupled bulk and interfacial diffusion for on-demand nanofiltration. *Nat. Commun.* **15**, 2282 (2024).
68. Z. Si, Z. Zhang, C. Yin, T. Ju, M. Wei, J. Huang, Y. Wang, Engineering transport highways in microporous membranes for lithium extraction: The double role of covalent organic frameworks. *J. Memb. Sci.* **680**, 121759 (2023).
69. X. Zhou, Z. Wang, R. Epsztein, C. Zhan, W. Li, J. D. Fortner, T. A. Pham, J.-H. Kim, M. Elimelech, Intrapore energy barriers govern ion transport and selectivity of desalination membranes. *Sci. Adv.* **6**, eabd9045 (2020).
70. S. V. Talekar, Temperature dependence of activation energies for self-diffusion of water and of alkali ions in aqueous electrolyte solutions. A model for ion selective behavior of biological cells. *Int. J. Quantum Chem.* **12**, 459–469 (1977).
71. C. Violet, A. Ball, M. Heiranian, L. F. Villalobos, J. Zhang, B. Uranlcan, H. Kulik, A. Haji-Akbari, M. Elimelech, Designing membranes with specific binding sites for selective ion separations. *Nat. Water* **2**, 706–718 (2024).
72. L. Cao, W. Guo, W. Ma, L. Wang, F. Xia, S. Wang, Y.-G. Wang, L. Jiang, D. Zhu, Towards understanding the nanofluidic reverse electrodialysis system: Well matched charge selectivity and ionic composition. *Energ. Environ. Sci.* **4**, 2259–2266 (2011).
73. M. K. Hazra, Y. Levy, Cross-talk of cation-π interactions with electrostatic and aromatic interactions: A salt-dependent trade-off in biomolecular condensates. *J. Phys. Chem. Lett.* **14**, 8460–8469 (2023).
74. P. Yang, L. Yang, Y. Wang, L. Song, J. Yang, G. Chang, An indole-based aerogel for enhanced removal of heavy metals from water via the synergistic effects of complexation and cation–π interactions. *J. Mater. Chem. A* **7**, 531–539 (2019).
75. Y. Qiang, S. Gao, Y. Zhang, S. Wang, L. Chen, L. Mu, H. Fang, J. Jiang, X. Lei, Thermally reduced graphene oxide membranes revealed selective adsorption of gold ions from mixed ionic solutions. *Int. J. Mol. Sci.* **24**, 12239 (2023).
76. B. Lyu, M. Wang, J. Jiang, Z. Jiang, Molecular design of covalent-organic framework membranes for $Li^+/Mg^{2+}$ separation: Significant charge effect. *J. Memb. Sci.* **662**, 120976 (2022).
77. M. Wang, W. Shen, X. Wang, G. Zhang, S. Zhao, F. Liu, The mixture effect on ionic selectivity and permeability of nanotubes. *Nanoscale Adv.* **2**, 3834–3840 (2020).
78. Z. Wang, K. Xiao, X.-M. Wang, Role of coexistence of negative and positive membrane surface charges in electrostatic effect for salt rejection by nanofiltration. *Desalination* **444**, 75–83 (2018).
79. A. Razmjou, G. Eshaghi, Y. Orooji, E. Hosseini, A. H. Korayem, F. Mohagheghian, Y. Boroumand, A. Noorbakhsh, M. Asadnia, V. Chen, Lithium ion-selective membrane with 2D subnanometer channels. *Water Res.* **159**, 313–323 (2019).
80. A. Lukum, E. Mohamad, A. D. K. Tangahu, S. Y. Ohi, Production and optimization of sea salt quality on the coast of Tomini bay. *J. Phys. Conf. Ser.* **1968**, 012013 (2021).
81. Jumaeri, T. Sulistyaningsih, D. Alighiri, Quality monitoring of salt produced in Indonesia through seawater evaporation on HDPE geomembrane lined ponds. *J. Phys. Conf. Ser.* **983**, 012166 (2018).
82. C. M. Rodrigues, A. Bio, F. Amat, N. Vieira, Artisanal salt production in aveiro/portugal - an ecofriendly process. *Saline Syst.* **7**, 3 (2011).
83. J.-M. Park, M.-H. Lee, S.-H. Lee, Characteristics and crystal structure of calcareous deposit films formed by electrodeposition process in artificial and natural seawater. *Coatings* **11**, 359 (2021).
84. M. J. Frisch, G. W. Trucks, H. B. Schlegel, G. E. Scuseria, M. A. Robb, J. R. Cheeseman, G. Scalmani, V. Barone, G. A. Petersson, H. Nakatsuji, X. Li, M. Caricato, A. Marenich, J. Bloino, B. G. Janesko, R. Gomperts, B. Mennucci, H. P. Hratchian, J. V. Ortiz, A. F. Izmaylov, J. L. Sonnenberg, D. Williams-Young, F. Ding, F. Lipparini, F. Egidi, J. Goings, B. Peng, A. Petrone, T. Henderson, D. Ranasinghe, V. G. Zakrzewski, J. Gao, N. Rega, G. Zheng, W. Liang, M. Hada, M. Ehara, K. Toyota, R. Fukuda, J. Hasegawa, M. Ishida, T. Nakajima, Y. Honda, O. Kitao, H. Nakai, T. Vreven, K. Throssell, J. A. Montgomery, Jr., J. E. Peralta, F. Ogliaro, M. Bearpark, J. J. Heyd, E. Brothers, K. N. Kudin, V. N. Staroverov, T. Keith, R. Kobayashi, J. Normand, K. Raghavachari, A. Rendell, J. C. Burant, S. S. Iyengar, J. Tomasi, M. Cossi, J. M. Millam, M. Klene, C. Adamo, R. Cammi, J. W. Ochterski, R. L. Martin, K. Morokuma, O. Farkas, J. B. Foresman, D. J. Fox, Gaussian 16, Revision B.01 (Gaussian Inc., 2016).
85. T. Lu, Molclus program, version 1.9.9.7 (2022); www.keinsci.com/research/molclus.html.
86. J. J. P. Stewart, Mopac: A semiempirical molecular orbital program. *J. Comput. Aided Mol. Des.* **4**, 1–103 (1990).
87. T. Lu, F. Chen, Multiwfn: A multifunctional wavefunction analyzer. *J. Comput. Chem.* **33**, 580–592 (2012).

88. W. Humphrey, A. Dalke, K. Schulten, VMD: Visual molecular dynamics. *J. Mol. Graph.* **14**, 33–38 (1996).
89. L. Wang, J. Zhao, F. Li, H. Fang, J. P. Lu, First-principles study of water chains encapsulated in single-walled carbon nanotube. *J. Phys. Chem. C* **113**, 5368–5375 (2009).
90. M. A. Matin, R. K. Chitumalla, M. Lim, X. Gao, J. Jang, Density functional theory study on the cross-linking of mussel adhesive proteins. *J. Phys. Chem. B* **119**, 5496–5504 (2015).
91. J. Wang, R. M. Wolf, J. W. Caldwell, P. A. Kollman, D. A. Case, Development and testing of a general amber force field. *J. Comput. Chem.* **25**, 1157–1174 (2004).
92. M. J. Robertson, Y. Qian, M. C. Robinson, J. Tirado-Rives, W. L. Jorgensen, Development and testing of the OPLS-AA/M force field for RNA. *J. Chem. Theory Comput.* **15**, 2734–2742 (2019).
93. T. Darden, D. York, L. Pedersen, Particle mesh Ewald: An *N*·log(*N*) method for Ewald sums in large systems. *J. Chem. Phys.* **98**, 10089–10092 (1993).
94. J. Kästner, Umbrella sampling. *Wiley Interdiscip. Rev. Comput. Mol. Sci.* **1**, 932–942 (2011).
95. C. Gu, D. Liu, W. Huang, J. Liu, R. Yang, Synthesis of covalent triazine-based frameworks with high $CO_2$ adsorption and selectivity. *Polym. Chem.* **6**, 7410–7417 (2015).
96. C. M. Thompson, G. Occhialini, G. T. McCandless, S. B. Alahakoon, V. Cameron, S. O. Nielsen, R. A. Smaldone, Computational and experimental studies on the effects of monomer planarity on covalent organic framework formation. *J. Am. Chem. Soc.* **139**, 10506–10513 (2017).
97. Z. Zhao, W. Chen, G. Zhang, Y. Chen, Interface molecular wires induce electron transfer from COFs to Pt for enhanced photocatalytic $H_2$ evolution. *J. Mater. Chem. A* **11**, 26052–26062 (2023).
98. S. Kandambeth, A. Mallick, B. Lukose, M. V. Mane, T. Heine, R. Banerjee, Construction of crystalline 2D covalent organic frameworks with remarkable chemical (acid/base) stability via a combined reversible and irreversible route. *J. Am. Chem. Soc.* **134**, 19524–19527 (2012).
99. J. Liu, F. Xu, J. Yuan, Z. Ji, Y. Zhao, F. Li, X. Guo, High-value conversion of $Na_2SO_4$ wastewater by a continuous electrodialytic metathesis process: Effects of coexisting ions. *J. Memb. Sci.* **615**, 118584 (2020).
100. J. Zhao, X. You, G. Wang, J. Yuan, Y. Li, C. Yang, S. Zhang, X. Wang, R. Zhang, H. Wu, Z. Jiang, Mix-charged polyamide membranes via molecular hybridization for selective ionic nanofiltration. *J. Memb. Sci.* **644**, 120051 (2022).
101. Z.-L. Qiu, W.-H. Yu, Y.-J. Shen, B.-K. Zhu, L.-F. Fang, Janus charged polyamide nanofilm with ultra-high separation selectivity for mono-/divalent ions. *Chem. Eng. J.* **416**, 129023 (2021).
102. C. Wu, S. Liu, Z. Wang, J. Zhang, X. Wang, X. Lu, Y. Jia, W.-S. Hung, K.-R. Lee, Nanofiltration membranes with dually charged composite layer exhibiting super-high multivalent-salt rejection. *J. Memb. Sci.* **517**, 64–72 (2016).
103. S. Liu, C. Wu, W.-S. Hung, X. Lu, K.-R. Lee, One-step constructed ultrathin Janus polyamide nanofilms with opposite charges for highly efficient nanofiltration. *J. Mater. Chem. A* **5**, 22988–22996 (2017).
104. G. Gong, P. Wang, Z. Zhou, Y. Hu, New insights into the role of an interlayer for the fabrication of highly selective and permeable thin-film composite nanofiltration membrane. *ACS Appl. Mater. Interfaces* **11**, 7349–7356 (2019).
105. X. Kong, M.-Y. Zhou, C.-E. Lin, J. Wang, B. Zhao, X.-Z. Wei, B.-K. Zhu, Polyamide/PVC based composite hollow fiber nanofiltration membranes: Effect of substrate on properties and performance. *J. Memb. Sci.* **505**, 231–240 (2016).
106. H. Li, W. Shi, Y. Zhang, Q. Du, X. Qin, Y. Su, Improved performance of poly(piperazine amide) composite nanofiltration membranes by adding aluminum hydroxide nanospheres. *Sep. Purif. Technol.* **166**, 240–251 (2016).
107. Y. Zhang, H. Wang, J. Guo, X. Cheng, G. Han, C. H. Lau, H. Lin, S. Liu, J. Ma, L. Shao, Ice-confined synthesis of highly ionized 3D-quasilayered polyamide nanofiltration membranes. *Science* **382**, 202–206 (2023).
108. B. Yuan, S. Zhao, P. Hu, J. Cui, Q. J. Niu, Asymmetric polyamide nanofilms with highly ordered nanovoids for water purification. *Nat. Commun.* **11**, 6102 (2020).
109. S. Han, J. Zhu, A. A. Uliana, D. Li, Y. Zhang, L. Zhang, Y. Wang, T. He, M. Elimelech, Microporous organic nanotube assisted design of high performance nanofiltration membranes. *Nat. Commun.* **13**, 7954 (2022).
110. Y. Zhang, R. Dong, U. R. Gabinet, R. Poling-Skutvik, N. K. Kim, C. Lee, O. Q. Imran, X. Feng, C. O. Osuji, Rapid fabrication by lyotropic self-assembly of thin nanofiltration membranes with uniform 1 nanometer pores. *ACS Nano* **15**, 8192–8203 (2021).
111. P. Sarkar, S. Modak, S. Karan, Ultraselective and highly permeable polyamide nanofilms for ionic and molecular nanofiltration. *Adv. Funct. Mater.* **31**, 2007054 (2021).
112. Z.-L. Qiu, L.-F. Fang, Y.-J. Shen, W.-H. Yu, B.-K. Zhu, C. Hélix-Nielsen, W. Zhang, Ionic dendrimer based polyamide membranes for ion separation. *ACS Nano* **15**, 7522–7535 (2021).
113. S. Gao, Y. Zhu, Y. Gong, Z. Wang, W. Fang, J. Jin, Ultrathin polyamide nanofiltration membrane fabricated on brush-painted single-walled carbon nanotube network support for ion sieving. *ACS Nano* **13**, 5278–5290 (2019).
114. G. Lu, S. Lu, J. Sun, M. W. Boey, W. Shang, J. Wu, A. K. An, Nano-confined supramolecular assembly of ultrathin crystalline polymer membranes for high-performance nanofiltration. *Adv. Funct. Mater.* **34**, 2309913 (2023).
115. Y. Han, Y. Jiang, C. Gao, High-flux graphene oxide nanofiltration membrane intercalated by carbon nanotubes. *ACS Appl. Mater. Interfaces* **7**, 8147–8155 (2015).
116. Y. Yang, X. Yang, L. Liang, Y. Gao, H. Cheng, X. Li, M. Zou, R. Ma, Q. Yuan, X. Duan, Large-area graphene-nanomesh/carbon-nanotube hybrid membranes for ionic and molecular nanofiltration. *Science* **364**, 1057–1062 (2019).
117. Z. Liu, Z. Ma, B. Qian, A. Y. H. Chan, X. Wang, Y. Liu, J. H. Xin, A facile and scalable method of fabrication of large-area ultrathin graphene oxide nanofiltration membrane. *ACS Nano* **15**, 15294–15305 (2021).
118. Y.-L. Ji, B.-X. Gu, S.-J. Xie, M.-J. Yin, W.-J. Qian, Q. Zhao, W.-S. Hung, K.-R. Lee, Y. Zhou, Q.-F. An, C.-J. Gao, Superfast water transport zwitterionic polymeric nanofluidic membrane reinforced by metal-organic frameworks. *Adv. Mater.* **33**, 2102292 (2021).
119. Y. Chen, T. Zhang, D. Chai, H. Ye, S. Tang, P. Wang, H. Sun, B. Ge, Q. J. Niu, Enhancing the NaCl/$Na_2SO_4$ separation selectivity and chlorine resistance of nanofiltration membranes by incorporating novel designed starch nanoparticles. *Appl. Surf. Sci.* **604**, 154417 (2022).
120. M. Jian, R. Qiu, Y. Xia, J. Lu, Y. Chen, Q. Gu, R. Liu, C. Hu, J. Qu, H. Wang, X. Zhang, Ultrathin water-stable metal-organic framework membranes for ion separation. *Sci. Adv.* **6**, eaay3998 (2020).
121. H. Wang, H. Wang, H. Jiang, A. Sheng, Z. Wei, Y. Li, C. Wu, H. Li, Positively charged polysulfonamide nanocomposite membranes incorporating hydrophilic triazine-structured COFs for highly efficient nanofiltration. *ACS Appl. Nano Mater.* **3**, 9329–9339 (2020).
122. R. Wang, M. Wei, Y. Wang, Secondary growth of covalent organic frameworks (COFs) on porous substrates for fast desalination. *J. Memb. Sci.* **604**, 118090 (2020).
123. Y. Zhang, J. Guo, G. Han, Y. Bai, Q. Ge, J. Ma, C. H. Lau, L. Shao, Molecularly soldered covalent organic frameworks for ultrafast precision sieving. *Sci. Adv.* **7**, eabe8706 (2021).
124. Y. Jiang, S. Li, J. Su, X. Lv, S. Liu, B. Su, Two dimensional COFs as ultra-thin interlayer to build TFN hollow fiber nanofiltration membrane for desalination and heavy metal wastewater treatment. *J. Memb. Sci.* **635**, 119523 (2021).
125. J. Shen, J. Yuan, B. Shi, X. You, R. Ding, T. Zhang, Y. Zhang, Y. Deng, J. Guan, M. Long, Y. Zheng, R. Zhang, H. Wu, Z. Jiang, Homointerface covalent organic framework membranes for efficient desalination. *J. Mater. Chem. A* **9**, 23178–23187 (2021).


**Acknowledgments:** We appreciate the assistance of Y. Qiu from Analytical Testing Center of the Department of Chemistry, Zhejiang University, in conducting GIWAXS measurements. **Funding:** This work was supported by the National Key Research and Development Program of China (2022YFA1503004), the National Science Foundation of China (22205198 and 21978274), the Experimental Technology Research Project of Zhejiang University (SYBJS202201), and the National Science Foundation of Zhejiang province (LR23B060001, LY22B06004, and LY23B060022). **Author contributions:** Conceptualization: Q.-W.M., S.M., Z.D., S.W., L.Z., H.Y., and Q.S. Methodology: Q.-W.M., F.C., H.Y., S.W., L.Z., and Q.S. Investigation: Q.-W.M., W.X., S.W., and L.Z. Visualization: Q.-W.M., Z.D., S.W., L.Z., and Q.S. Writing—original draft: Q.-W.M., Z.D., S.W., L.Z., and Q.S. Writing—review and editing: Q.-W.M., S.W., L.Z., and Q.S. Validation: Q.-W.M., J.L., Z.L., Z.D., L.Z., S.W., and Q.S. Formal analysis: Q.-W.M., J.L., S.W., L.Z., and Q.S. Software: J.L. Project administration: Q.-W.M., S.W., L.Z., and Q.S. Data curation: Q.-W.M., L.Z., and S.W. Funding acquisition: Q.-W.M., L.Z., S.W., and Q.S. Resources: Q.-W.M., Z.D., S.W., L.Z., and Q.S. Supervision: Q.S. **Competing interests:** The authors declare that they have no competing interests. **Data and materials availability:** All data needed to evaluate the conclusions in the paper are present in the paper and/or the Supplementary Materials.

Submitted 24 February 2024
Accepted 21 August 2024
Published 25 September 2024
10.1126/sciadv.ado8658